Nucleon binding energy and transverse momentum imbalance in neutrino-nucleus reactions

T. Cai,[1] X.-G. Lu,[2] L. A. Harewood,[3] C. Wret,[1] F. Akbar,[4] D. A. Andrade,[5] M. V. Ascencio,[6] L. Bellantoni,[7] A. Bercellie,[1] M. Betancourt,[7] A. Bodek,[1] J. L. Bonilla,[5] A. Bravar,[8] H. Budd,[1] G. Caceres,[9] M. F. Carneiro,[10] D. Coplowe,[2] H. da Motta,[9] Zubair Ahmad Dar,[4] G. A. Díaz,[1,6] J. Felix,[5] L. Fields,[7,11] A. Filkins,[12] R. Fine,[1] A. M. Gago,[6] H. Gallagher,[13] A. Ghosh,[14,9] R. Gran,[3] D. A. Harris,[15,7] S. Henry,[1] S. Jena,[16] D. Jena,[7] J. Kleykamp,[1] M. Kordosky,[12] D. Last,[17] T. Le,[13,18] A. Lozano,[9] E. Maher,[19] S. Manly,[1] W. A. Mann,[13] C. Mauger,[17] K. S. McFarland,[1] B. Messerly,[20] J. Miller,[14] J. G. Morfín,[7] D. Naples,[20] J. K. Nelson,[12] C. Nguyen,[21] A. Norrick,[12] Nuruzzaman,[18,14] A. Olivier,[1] V. Paolone,[20] G. N. Perdue,[7,1] M. A. Ramírez,[5] R. D. Ransome,[18] D. Ruterbories,[1] H. Schellman,[10,11] C. J. Solano Salinas,[22] H. Su,[20] M. Sultana,[1] V. S. Syrotenko,[13] E. Valencia,[12,5] D. Wark,[2] A. Weber,[2] M. Wospakrik,[21] B. Yaeggy,[14] and L. Zazueta[12]

(The MINERνA Collaboration)

[1]*University of Rochester, Rochester, New York 14627, USA*
[2]*Oxford University, Department of Physics, Oxford, United Kingdom*
[3]*Department of Physics, University of Minnesota—Duluth, Duluth, Minnesota 55812, USA*
[4]*AMU Campus, Aligarh, Uttar Pradesh 202001, India*
[5]*Campus León y Campus Guanajuato, Universidad de Guanajuato, Lascurain de Retana No. 5, Colonia Centro, Guanajuato 36000, Guanajuato, México*
[6]*Sección Física, Departamento de Ciencias, Pontificia Universidad Católica del Perú, Apartado 1761, Lima, Perú*
[7]*Fermi National Accelerator Laboratory, Batavia, Illinois 60510, USA*
[8]*University of Geneva, 1211 Geneva 4, Switzerland*
[9]*Centro Brasileiro de Pesquisas Físicas, Rua Dr. Xavier Sigaud 150, Urca, Rio de Janeiro, Rio de Janeiro, 22290-180, Brazil*
[10]*Department of Physics, Oregon State University, Corvallis, Oregon 97331, USA*
[11]*Northwestern University, Evanston, Illinois 60208, USA*
[12]*Department of Physics, College of William & Mary, Williamsburg, Virginia 23187, USA*
[13]*Physics Department, Tufts University, Medford, Massachusetts 02155, USA*
[14]*Departamento de Física, Universidad Técnica Federico Santa María, Avenida España 1680 Casilla 110-V, Valparaíso, Chile*
[15]*York University, Department of Physics and Astronomy, Toronto, Ontario M3J 1P3, Canada*
[16]*IISER, Mohali, Knowledge city, Sector 81, Manauli PO 140306 Punjab, India*
[17]*Department of Physics and Astronomy, University of Pennsylvania, Philadelphia, Pennsylvania 19104, USA*
[18]*Rutgers, The State University of New Jersey, Piscataway, New Jersey 08854, USA*
[19]*Massachusetts College of Liberal Arts, 375 Church Street, North Adams, Massachusetts 01247, USA*
[20]*Department of Physics and Astronomy, University of Pittsburgh, Pittsburgh, Pennsylvania 15260, USA*
[21]*University of Florida, Department of Physics, Gainesville, Florida 32611, USA*
[22]*Universidad Nacional de Ingeniería, Apartado 31139, Lima, Perú*

(Received 22 October 2019; revised manuscript received 16 March 2020; accepted 16 April 2020; published 1 May 2020)

We have measured new observables based on the final state kinematic imbalances in the mesonless production of $\nu_\mu + A \to \mu^- + p + X$ in the MINERνA tracker. Components of the muon-proton momentum imbalances parallel (δp_{Ty}) and perpendicular (δp_{Tx}) to the momentum transfer in the transverse plane are found to be sensitive to the nuclear effects such as Fermi motion, binding energy, and non-quasielastic (QE) contributions. The QE peak location in δp_{Ty} is particularly sensitive to the binding energy. Differential cross sections are compared to predictions from different neutrino interaction models. The Fermi gas models presented in this study cannot simultaneously describe features such as QE

peak location, width, and the non-QE events contributing to the signal process. Correcting the GENIE's binding energy implementation according to theory causes better agreement with data. Hints of proton left-right asymmetry are observed in δp_{Tx}. Better modeling of the binding energy can reduce the bias in neutrino energy reconstruction, and these observables can be applied in current and future experiments to better constrain nuclear effects.

DOI: 10.1103/PhysRevD.101.092001

I. INTRODUCTION

Neutrino oscillation experiments measure the final state particles produced by neutrino-nucleus scattering processes. Models that accurately describe these interactions are crucial to reducing the uncertainties in the measurements of oscillation parameters.

Most neutrino-nucleus interactions are modeled through the impulse approximation (IA), where the probe sees the target nucleus as a collection of independent nucleons and the resulting particles then evolve independently. Important components of modeling in the IA picture include the initial state nucleon's energy-momentum distributions, the nuclear potentials, and the final state interactions (FSIs) that modify the kinematics of the final-state particles as they propagate through the nucleus.

The leptonic system provides energy to the hadronic side of the reaction to bring a bound nucleon on shell and separate it from the remnant nucleus. Such energy is often loosely referred to as "binding energy", but Ref. [1] draws a distinction between the different energy parameters in neutrino models and how their effects depend on the implementation details.

In this paper, we refer to the average energy transferred to the target nucleus to bring a bound nucleon inside the target onto the mass shell as the "removal energy," represented in this paper by $\epsilon^{N(P)}$ for the neutron (proton) initial state in neutrino (antineutrino) interactions. The energy associated with nuclear potentials is referred to as the nuclear potential energy. The combined effects of the "removal energy" and the nuclear potential energy is referred to as the "interaction energy". The interaction energy implementation in the IA picture is discussed in detail in Sec. II.

For many neutrino experiments, particularly at low energies like T2K, MicroBooNE, and the second oscillation maximum in DUNE, incorrect treatment of the interaction energy may significantly bias the reconstructed neutrino energy and will alter the expected kinematics of final state nucleons. Such effects are already a significant systematic in the measurement of δm^2_{23} in the T2K experiment [1,2].

This paper will examine a set of new observable quantities that are sensitive to nuclear effects and especially to the interaction energy implementation used in generators. The variables are extensions to the recent measurements of momentum imbalance in mesonless events with a muon and proton in the final state, here referred to as single transverse kinematic imbalance (single-TKI) [3] by the MINERνA [4] and T2K [5] experiments.

The new observables are derived from the single-TKI observable $\delta\mathbf{p}_{\mathrm{T}}$. Specifically, we define δp_{Ty} to be the projection of $\delta\mathbf{p}_{\mathrm{T}}$ along the transverse component of the leptonic momentum transfer, which is sensitive to the effects of the interaction energy. We also report on the cross section in δp_{Tx}, the $\delta\mathbf{p}_{\mathrm{T}}$ projection normal to the neutrino-muon interaction plane. The single-TKI variables and their sensitivities to the interaction energy is discussed in greater details in Sec. III and Sec. IV, respectively.

These quantities provide neutrino oscillation experiments with a method to evaluate the validity of the interaction energy implemented in the interaction models. The interaction energy affects the reconstructed energy scale in the simulated neutrino interaction. Evaluating the uncertainties in the neutrino energy scale based on an inaccurate implementation of the interaction energy will result in unnecessarily large systematics.

We measure δp_{Tx} and δp_{Ty} using MINERνA ν_μ-induced muon-proton mesonless interactions on a hydrocarbon at $\langle E_\nu \rangle = 3$ GeV; this is the same data set as was studied previously in Ref. [4]. The differential cross sections in these quantities are compared with GENIE [6], NEUT 5.40 [7], NuWro [8], and GiBUU [9,10] event generator predictions. The methodology is detailed in Sec. V, and the results are discussed in Sec. VI.

II. IMPULSE APPROXIMATION

We illustrate the effects of interaction energy with the charged-current quasielastic (CCQE) interaction in the IA picture shown in Fig. 1. In this picture, only a single nucleon is involved in the hard scattering, $\nu\mathrm{n} \to \mu^-\mathrm{p}$.

The neutrino with energy E_0 made the four-momentum transfer, $q = (q_0, \mathbf{q_3})$ to a bound neutron of mass M_N inside a target nucleus with A nucleons, where q_0 and $\mathbf{q_3}$ are the energy and momentum transfer, respectively. The target nucleus was initially at rest with mass M_{A}, the bound neutron has a four-momentum $E_i = (M_N - \epsilon^N, \mathbf{k})$, where $\mathbf{k}$ is neutron's Fermi momentum. The remnant nucleus with a four-momentum P^*_{A-1} must have momentum $-\mathbf{k}$ for the target nucleus to be at rest. The energy of the initial state neutron can be written as

$$E_i = M_{\mathrm{A}} - \sqrt{{M^*_{\mathrm{A-1}}}^2 + \mathbf{k}^2}, \tag{1}$$

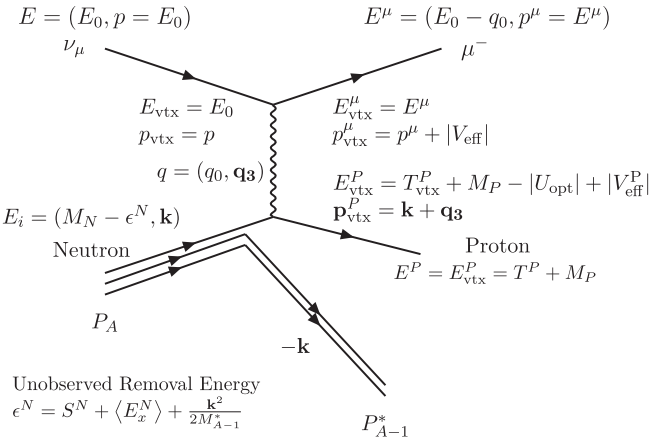

FIG. 1. A neutrino interaction with a bound neutron in the impulse approximation. ν, μ, N, and P are the neutrino, muon, neutron, and protons, respectively. The incoming neutrino with four-momentum E interacts with the bound neutron with three-momentum $\mathbf{k}$ and removal energy ϵ^N. The removal energy consists of the nucleon separation energy S^N, average excitation energy $\langle E^N_x \rangle$, and the kinetic energy of the remnant nucleus. $E^{P(\mu)}$ and $p^{P(\mu)}$ are the proton (μ) total energy and momentum, T^P is the proton kinetic energy, $|U_{\rm opt}|$, and $|V^{\rm P}_{\rm eff}|$ ($|V_{\rm eff}|$) are the magnitudes of the optical potential and the Coulomb potential experienced by proton (muon). The quantities with the subscript (vtx) are those immediately after four-momentum transfer.

where $M^*_{\rm A-1}$ is the mass of the excited spectator nucleus. For the nuclear targets typically used in neutrino experiments (^{12}C, ^{16}O, and ^{40}Ar), we have $M^*_{\rm A-1}{}^2 \gg \mathbf{k}^2$. Then we can expand the initial state nucleon energy as

$$E_i \approx M_{\rm A} - M^*_{\rm A-1} - \frac{\mathbf{k}^2}{2M^*_{\rm A-1}} = M_N - S^N - E^N_x - \frac{\mathbf{k}^2}{2M^*_{\rm A-1}}. \quad (2)$$

The removal energy parameter,

$$\epsilon^N = S^N + E^N_x + \langle T_{A-1} \rangle, \quad (3)$$

accounts for the *neutron separation energy* from the target nucleus S^N,

$$S^N = M_{A-1} + M_N - M_A, \quad (4)$$

and the excitation energy of the final state nucleus, E^N_x, when the initial state nucleon is a neutron,

$$E^N_x = M^*_{A-1} - M_{A-1}. \quad (5)$$

The average kinetic energy $\langle T_{A-1} \rangle = \mathbf{k}^2/(2M^*_{\rm A-1})$ of the excited remnant nucleus with A-1 nucleons affects the interaction only through its nuclear potentials. For neutrino QE interactions on ^{12}C, $S^N = 18.7$ MeV, $E^N_x = 10.1$ MeV, and $\langle T_{A-1} \rangle = 1.4$ MeV [1]. The removal energy is the average energy needed to bring the neutron onto the mass shell.

There are additional effects associated with the nuclear potentials that should be accounted for. For example, the nuclear optical potential describes the nucleus as a medium with a complex refractive index: the real part of the potential affects the allowed kinematics of the initial state lepton-nucleon system in the IA while the imaginary part is related to inelastic scattering as the outgoing nucleon is making an exit from the nucleus [11]. Reference [1] fits inclusive electron scattering data to determine the real part of the optical potential, which depends on the three momentum of the outgoing nucleon at the interaction vertex. This optical potential is denoted as $U_{\rm opt}[(\mathbf{k} + \mathbf{q}_3)^2]$ in this work. The effect of the optical potential is largest at lower momentum. For carbon, the parametrization of Ref. [1] is

$$U_{\rm opt} = \min[0, -29.1 + (40.9/{\rm GeV}^2)(\mathbf{k} + \mathbf{q}_3)^2)]\ {\rm MeV}. \quad (6)$$

In this analysis, we use this parametrization, and it is on average 2 MeV for our selected events.

Another potential, the Coulomb potential $V_{\rm eff}$ of the positively charged remnant nucleus will modify the momenta of the outgoing charged particles as they propagate through the nucleus. In Fig. 1, a distinction between the Coulomb potential experienced by muon ($|V_{\rm eff}|$) and proton ($|V^{\rm P}_{\rm eff}|$) is made; however, for neutrino interactions, both particles experience the same Coulomb potential as the proton number in the nucleus remains unchanged after the interaction. For carbon, $|V_{\rm eff}|$ is 3.1 MeV [1].

Figure 1 illustrates energy and momentum conservation between the initial and final state. The total energy of the final proton and muon is equal to the total of the initial neutron and lepton, less the energy required to create the final state excited nucleon in the reaction. The Coulomb potential affects any charged final state particles, but the optical potential affects the final state nucleon only. For example, the muon with the total energy $E^\mu = E^\mu_{\rm vtx}$ begins inside the Coulomb potential, with kinetic energy $E^\mu + |V_{\rm eff}|$ and potential energy $-|V_{\rm eff}|$, and is decelerated during transport inside the nucleus medium so that its kinetic energy is E^μ outside the nucleus. The proton experiences both the Coulomb potential and the optical potential, which modify its kinetic energy and momentum but conserve the total energy. The full energy conservation equation on the hadronic side is as follows [1]:

$$E^P_{\rm vtx} = q_0 + M_N - S^N - E^N_x - \frac{\langle \mathbf{k}^2 \rangle}{2M^*_{A-1}{}^2} = \sqrt{(\mathbf{k} + \mathbf{q_3})^2 + M_P^2} - |U_{\rm opt}[(\mathbf{k} + \mathbf{q_3})^2]| + |V^{\rm P}_{\rm eff}| = E^P. \quad (7)$$

Here, the final state proton is assumed to be on shell with energy $E^P_{\rm vtx} = E^P_f$, before and after exiting the nucleus. Its kinetic energy immediately after the four-momentum transfer is

$$T^P_{\rm vtx} = q_0 + M_N - M_P - \epsilon^N \tag{8}$$

and is modified by the nuclear potentials so that outside the nucleus the kinetic energy becomes

$$T^P = T^P_{\rm vtx} - |U_{\rm opt}| + |V^{\rm P}_{\rm eff}|. \tag{9}$$

The removal energy used by neutrino Monte Carlo (MC) generators, such as GENIE [6], NEUT [7], and NuWro [8], are discussed in detail in Ref. [1]. These generators use variants of spectral functions, mostly the Fermi gas model in the IA picture with removal energy constrained by inclusive electron scattering data [12]. However, they have distinct implementations of the IA model which affects the energy terms going into the removal energy parameter. For example, in GENIE's IA implementation, the off shell bound initial nucleon is generated with Eq. (7), but with E^N_x, $U_{\rm opt}$, and $V^{\rm P}_{\rm eff}$ set to 0. GENIE subtracts an additional "binding energy" parameter $\Delta^{\rm nucleus}_{\rm GENIE}$ from the final state protons in QE processes to account for the removal energy. The implementation of this term is independent of the kinematics at the interaction vertex, which causes the energy of the final state nucleons to be biased. The values of $\Delta^{\rm nucleus}_{\rm GENIE}$ were measured by Ref. [12] and referred to as the "Moniz interaction energy" in Ref. [1]. The Moniz interaction energy is an empirical fit to the sum of the removal energy and the nuclear potentials, but for a nonrelativistic on shell formalism. For $\nu + {}^{12}$C scattering, $\Delta^{\rm C}_{\rm GENIE} = 25$ MeV [6].

In this paper, we refer to the collective energy shifts due to removal energy and the nuclear potentials as the "interaction energy", in the spirit of the Moniz interaction energy of Ref. [1]. This interaction energy is specific to the off shell formalism described in Eq. (7).

We simulate the effects of the interaction energy implementations in GENIE by modifying the final state muon and proton energies after a sample is generated according to Table I. The corrections outlined are motivated by the study in Ref. [1]. Comparisons between the default GENIE implementation (0 in Table I) and two different corrections (1 and 2) are made. For both sets of corrections, which are applied to QE events, we add $\Delta^{\rm C}_{\rm GENIE}$ back to the exiting proton to undo the bias, we then subtract E_x from the muon to account for the shift in momentum transfer in the leptons (derived in Appendix A). In addition, the correction 1 applies an optical potential correction to both the muon and proton, while the correction 2 applies the Coulomb correction on top of correction 1. The average $|U_{\rm opt}|$ is $\approx$2 MeV for the proton and muon kinematics chosen.

The corrections are approximations, which implement the leading effect of the nuclear potential. That potential will also cause changes, small for our events that have an energetic final state proton, in the four momentum transferred to the off shell target nucleon. Appendix A provides the derivation of our corrections.

III. THE SINGLE-TKI VARIABLES

The single-TKI measurements for CCQE-like events, which include a lepton, at least one proton, and no mesons in the final state, are defined in Ref. [3],

$$\delta\mathbf{p}_{\rm T} \equiv \mathbf{p}^{\rm p}_{\rm T} + \mathbf{p}^{\mu}_{\rm T}, \tag{10}$$

$$\delta\alpha_{\rm T} \equiv \arccos\left(-\hat{\mathbf{p}}^{\mu}_{\rm T} \cdot \hat{\delta}\mathbf{p}_{\rm T}\right), \tag{11}$$

where $\mathbf{p}^{\rm p}_{\rm T}$ and $\mathbf{p}^{\mu}_{\rm T}$ are the components of proton and muon momenta in the plane perpendicular to the neutrino direction. The single-TKI variable $\delta\mathbf{p}_{\rm T}$ and its decompositions along the Cartesian coordinate system defined with respect to the neutrino and muon kinematics are illustrated in Fig. 2 and mathematically defined as

$$\begin{aligned} \delta p_{\rm Tx} &= (\hat{\mathbf{p}}_\nu \times \hat{\mathbf{p}}^{\mu}_{\rm T}) \cdot \delta\mathbf{p}_{\rm T}, \\ \delta p_{\rm Ty} &= -\hat{\mathbf{p}}^{\mu}_{\rm T} \cdot \delta\mathbf{p}_{\rm T}. \end{aligned} \tag{12}$$

Here, $\hat{\mathbf{p}}_\nu$ is the neutrino direction, $\delta p_{\rm Ty}$ is antiparallel to the muon transverse direction $\hat{\mathbf{p}}^{\mu}_{\rm T}$ while $\delta p_{\rm Tx}$ is perpendicular to $\delta p_{\rm Ty}$ along the normal of neutrino-muon plane. The coordinate system describing $\delta p_{\rm Tx}$ and $\delta p_{\rm Ty}$ is relative to the neutrino and muon kinematics. Specifically, $\hat{\mathbf{y}}$ is along the transverse component of three-momentum transfer, $\hat{\mathbf{z}}$ is along the neutrino direction, and there is no three-momentum transfer in the $\hat{\mathbf{x}}$ direction. Both $\delta p_{\rm Tx}$ and $\delta p_{\rm Ty}$ can be measured from the final state particles. Any interaction energy effect will mostly affect the four-momentum

TABLE I. Calculated energy corrections to the final state leptons and hadrons from the GENIE generator for QE neutrino scattering on ${}^{12}C$, $\Delta^{\rm C}_{\rm GENIE} = 25$ MeV, $E_x = 10.1$ MeV. Other interaction channels are not altered.

Correction	$E^P = E^P_{\rm GENIE} + \delta^P$ δ^P(MeV)	$E^\mu = E^\mu_{\rm GENIE} + \delta^\mu$ δ^μ(MeV)	GENIE baseline shift, $\langle\delta^\mu\rangle, \langle\delta^\mu\rangle$ (MeV)	QE baseline shift $\langle\delta p_{\rm Ty}\rangle$(MeV/$c$)
0: Default (no corrections)	0	0	0,0	0
1: $U_{\rm opt}$ only (w/ E_x&$\Delta^{\rm C}_{\rm GENIE}$)	$\Delta^{\rm C}_{\rm GENIE} - \lvert U_{\rm opt}\rvert$	$\lvert U_{\rm opt}\rvert - E_x$	22.7, −7.8	29.4
2: $U_{\rm opt}$ and $V_{\rm eff}$ (w/ E_x&$\Delta^{\rm C}_{\rm GENIE}$)	$\Delta^{\rm C}_{\rm GENIE} - \lvert U_{\rm opt}\rvert + \lvert V^{\rm P}_{\rm eff}\rvert$	$\lvert U_{\rm opt}\rvert - E_x - \lvert V_{\rm eff}\rvert$	25.8, −10.9	33.9

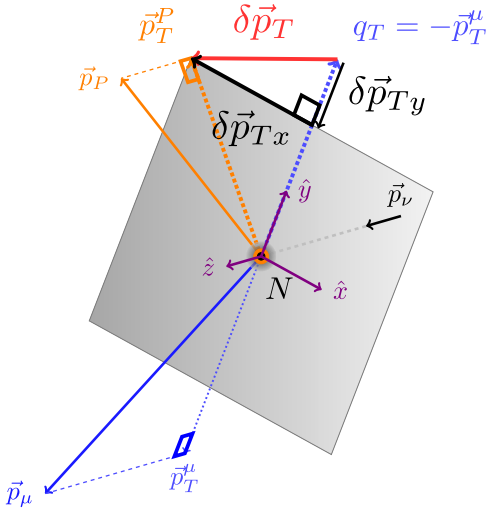

FIG. 2. Schematics of the single transverse kinematic imbalances and their projections.The incoming neutrino interacts on the neutron (N) in the nucleus. The neutrino direction $\hat{\mathbf{p}}_\nu$ forms the z axis. A final state muon with $\mathbf{p}_\mu$ and a proton with $\mathbf{p}_p$ are produced. The muon transverse momentum is $\mathbf{p}_{\mathrm{T}}^{\mu}$, and $-\hat{\mathbf{p}}_{\mathrm{T}}^{\mu}$ defines the y axis. The proton transverse momentum is $\mathbf{p}_{\mathrm{T}}^{\mathrm{p}}$ and decomposed along x and y axis, respectively. In this example, both δp_{Tx} and δp_{Ty} are negative, and only the distribution of δp_{Tx} for QE events is expected to be symmetric around zero.

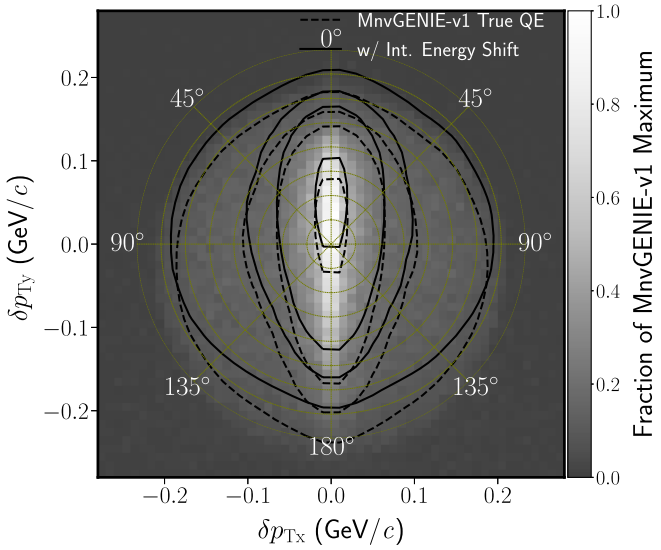

FIG. 3. δp_{Ty} vs δp_{Tx} for CCQE events in GENIE. The contours, from outside towards the center, represent 0.1, 0.2, 0.3, and 0.7 of maximum. The angles correspond to $\delta\alpha_{\mathrm{T}}$ values. The neutrino direction points out of the page. The dashed contour describes the default GENIE distribution with a MnvGENIE-v1 tune, described in Sec. V. The solid contour shows the shift in the distribution after correction is made to the interaction energy with correction 01 of Table I. There is negligible deformation in the δp_{Tx} direction compared to the shift in δp_{Ty}.

transfer and δp_{Ty}. For CCQE events, δp_{Tx} is expected to symmetrically distribute on both sides of the neutrino-muon interaction plane.

$(\delta p_{\mathrm{Tx}}, \delta p_{\mathrm{Ty}})$ can be defined in terms of $(\delta p_{\mathrm{T}}, \delta\alpha_{\mathrm{T}})$ as

$$|\delta p_{\mathrm{Tx}}| = \delta p_{\mathrm{T}} \sin\delta\alpha_{\mathrm{T}},$$
$$\delta p_{\mathrm{Ty}} = \delta p_{\mathrm{T}} \cos\delta\alpha_{\mathrm{T}}. \tag{13}$$

Here, δp_{Ty} is positive if the proton has gained momentum along $-\mathbf{p}_{\mathrm{T}}^{\mu}$. Figure 3 illustrates the relationship between $(\delta p_{\mathrm{Tx}}, \delta p_{\mathrm{Ty}})$ and $(\delta p_{\mathrm{T}}, \delta\alpha_{\mathrm{T}})$ as the different projections of $\delta\mathbf{p}_{\mathrm{T}}$ in the Cartesian and the polar coordinate systems, respectively. The resulting distribution in the $\delta\alpha_{\mathrm{T}}$ and δp_{T} residuals provides insights into other nuclear effects affecting the cross section, such as FSIs, the Fermi motion, and two-particle-two-hole (2p2h) processes [4].

IV. SENSITIVITIES TO INTERACTION ENERGY IMPLEMENTATION

The shapes of δp_{Tx} and δp_{Ty} are affected by nuclear effects. The nonzero width of δp_{Tx} for the QE portion of the signal is largely due to the Fermi motion of the target nucleus. The average Fermi momentum in carbon is approximately 221 MeV. In the absence of FSI effects, this is the only momentum available in the x direction. FSIs could alter the outgoing protons' directions, but in carbon, an outgoing nucleon typically exits without interacting with the nucleus or interacts with the nucleus elastically producing a small change in direction.

The momentum transferred to the hadronic system is confined in the yz plane. On an event by event basis, the nuclear potential may alter this momentum as well, and therefore, the direction of the final state nucleon, but this effect averages to zero because the initial state nuclear momentum is on average zero. Therefore, changes to the interaction energy at the event vertex, on average, only alter δp_{Ty}. Mathematically, the effect of the interaction energy is as follows:

For an outgoing nucleon with energy E_f' before it has left the region of nuclear potentials, its momentum $\mathbf{p}_f$ as a function of an energy shift τ due to the interaction energy is

$$|\mathbf{p}_f(\tau)| = \sqrt{(E_f' - \tau)^2 - M_P^2}, \tag{14}$$

where $E_f' = \sqrt{M_P^2 + \mathbf{p}_0^2}$ and $\mathbf{p}_0 = \mathbf{p}_f(0) = \mathbf{k} + \mathbf{q}$. In the limit,

$$\frac{\tau E_f'}{p_0^2} \ll 1, \tag{15}$$

we can approximate $\mathbf{p}_f(\tau)$ by

$$\mathbf{p}_f(\tau) \approx \left(1 - \frac{E_f'}{p_0^2}\tau\right)\mathbf{p}_0. \tag{16}$$

Defining $\alpha = \tau E'_f/p_0^2$, we can write the 4-momentum conservation equation without FSI as

$$\begin{pmatrix} q_0 \\ 0 \\ q_T \\ q_L \end{pmatrix} + \begin{pmatrix} E_i \\ k_x \\ k_y \\ k_z \end{pmatrix} \approx \begin{pmatrix} E'_f \\ p_{0x} \\ p_{0y} \\ p_{0z} \end{pmatrix} - \begin{pmatrix} \tau \\ \alpha p_{0x} \\ \alpha p_{0y} \\ \alpha p_{0z} \end{pmatrix}, \quad (17)$$

where $(0, q_T, q_L)$ are components of the three-momentum transfer $\mathbf{q}$, (k_x, k_y, k_z) are components of Fermi motion $\mathbf{k}$. In this picture, q_T is directly measurable as the transverse component of muon momentum, with magnitude p_{T}^{μ}, but q_L cannot be directly measured and estimates depend on the model used to calculate neutrino energy.

The transverse components of the three-momentum imbalance are

$$\delta p_{\mathrm{Tx}} = (1-\alpha)p_{0x} \approx k_x - \alpha p_{0x} = k_x - \tau \frac{E_f}{p_0^2} p_{0x}, \quad (18)$$

$$\begin{aligned} \delta p_{\mathrm{Ty}} &= (1-\alpha)p_{0y} + \mathbf{p}_{\mu} \cdot \hat{\mathbf{y}} \\ &= p_{0y} - p_T^{\mu} - \alpha p_{0y} = p_{0y} - q_T - \alpha p_{0y} \\ &\approx k_y - \alpha p_{0y} = k_y - \tau \frac{E_f}{p_0^2} p_{0y}, \end{aligned} \quad (19)$$

where we have assumed $k_x \approx p_{0x}$ and $q_T + k_y \approx p_{0y}$ because the Fermi momentum is large compared to the interaction energy-induced change in momentum. In the limit $\tau, \alpha \to 0$, δp_{Tx}, and δp_{Ty} are the transverse components of the Fermi momentum, (k_x, k_y). The effect of the energy shift, τ, in each component of $(\delta p_{\mathrm{Tx}}, \delta p_{\mathrm{Ty}})$ is then proportional to that component of p_0. When $p_T^{\mu} \gg k_y$, the shift in δp_{Ty} will be larger than the shift in δp_{Tx}. In both components, the interaction energy effects acting on the Fermi momentum will average to zero, whereas the effects on δp_{Ty} from q_T will yield a net average shift in δp_{Ty}. For events in GENIE2.12.10, there is approximately an $+15$ MeV/c offset in δp_{Ty}. The last column in Table I shows how applying energy corrections to the final state proton affects the average QE peak positions in δp_{Ty}.

V. APPARATUS AND METHODOLOGY

The measurements of differential cross sections in δp_{Tx} and δp_{Ty} with the MINERνA detector [13] use the same sample and methodology of the measurements described in Ref. [4]. The signal requires no pions, one muon, and at least one proton in the final state, satisfying

$$1.5\ \mathrm{GeV}/c < p_{\mu} < 10\ \mathrm{GeV}/c, \qquad \theta_{\mu} < 20°, \quad (20)$$

$$0.45\ \mathrm{GeV}/c < p_{\mathrm{p}} < 1.2\ \mathrm{GeV}/c, \qquad \theta_{\mathrm{p}} < 70°, \quad (21)$$

where p_{μ} and θ_{μ} (p_{p} and θ_{p}) are the final-state muon (proton) momentum and opening angle with respect to the neutrino direction, respectively. The data set corresponds to 3.28×10^{20} protons on target (POT) delivered between 2010 and 2012 by the NuMI beam line [14] at Fermilab. For this beam, the integrated ν_{μ} flux is predicted to be $2.88 \times 10^{-8}/\mathrm{cm}^2/\mathrm{POT}$ [15].

Neutrino interactions are simulated with GENIE 2.8.4 [6] in both a nominal form, and also with a MINERνA "tune" (MnvGENIE-v1.0.1). The nominal GENIE generates initial states with a modified Fermi gas model containing contributions from the Bodek-Ritchie tail [16]. The CCQE cross section is produced by the Llewellyn Smith formalism [17], with a dipole axial form factor with axial mass $M_A^{\mathrm{QE}} = 0.99\ \mathrm{GeV}/c^2$. Resonant pion production is modeled by the Rein-Sehgal [18] model. Deep inelastic scattering is simulated with a quark-parton model parametrized with the Bodek-Yang structure functions [19]. FSI is simulated with the GENIE hA model.

The tuning is based on MnvGENIE-v1, which has been applied in previous publications [4,20,21]. MnvGENIE-v1 includes the Valencia two-particle-two-holes (2p2h) model [22–24] for two-body current simulation. Furthermore, the interaction strength of this 2p2h model has been tuned to MINERνA inclusive scattering data [25], resulting in a significant enhancement relative to the Valencia model in a restricted region of energy-momentum transfer. MnvGENIE-v1 also includes a nonresonant pion reduction to 43% of the nominal as constrained by comparisons with bubble chamber deuterium data [26,27]. There is also a modification to the collective excitations of the nucleus for the CCQE channel, approximated as a superposition of 1p1h excitations and calculated with the random phase approximation (RPA) in Ref. [28] and uncertainties in Ref. [29]. The effects of nonresonant pion production and RPA in this analysis are negligible.

On top of the MnvGENIE-v1 tuning, MnvGENIE-v1.0.1 removes QE events with elastic nucleon-nucleus FSI, replacing them with events where there is no FSI, to remove the effect of a mistake in GENIEś implementation of the elastic nucleon-nucleus FSI. The primary effect in the final state is in the angular distribution of outgoing protons. A detailed discussion of this mistake can be found in Appendix B.

Reconstructed events with one muon and at least one proton in the MINERνA tracker satisfying Eqs. (20) and (21) are selected. Figure 4 shows the reconstruction efficiencies of the muons and the protons due to event selection and detector acceptance.

Only the muons which exit from the back of the MINERνA detector and end up in the MINOS detector can be fully reconstructed. The muon momentum lost inside MINERνA is measured by energy deposits. The momentum in MINOS is estimated by range or curvature, which depends on whether the muon is contained in the MINOS spectrometer.

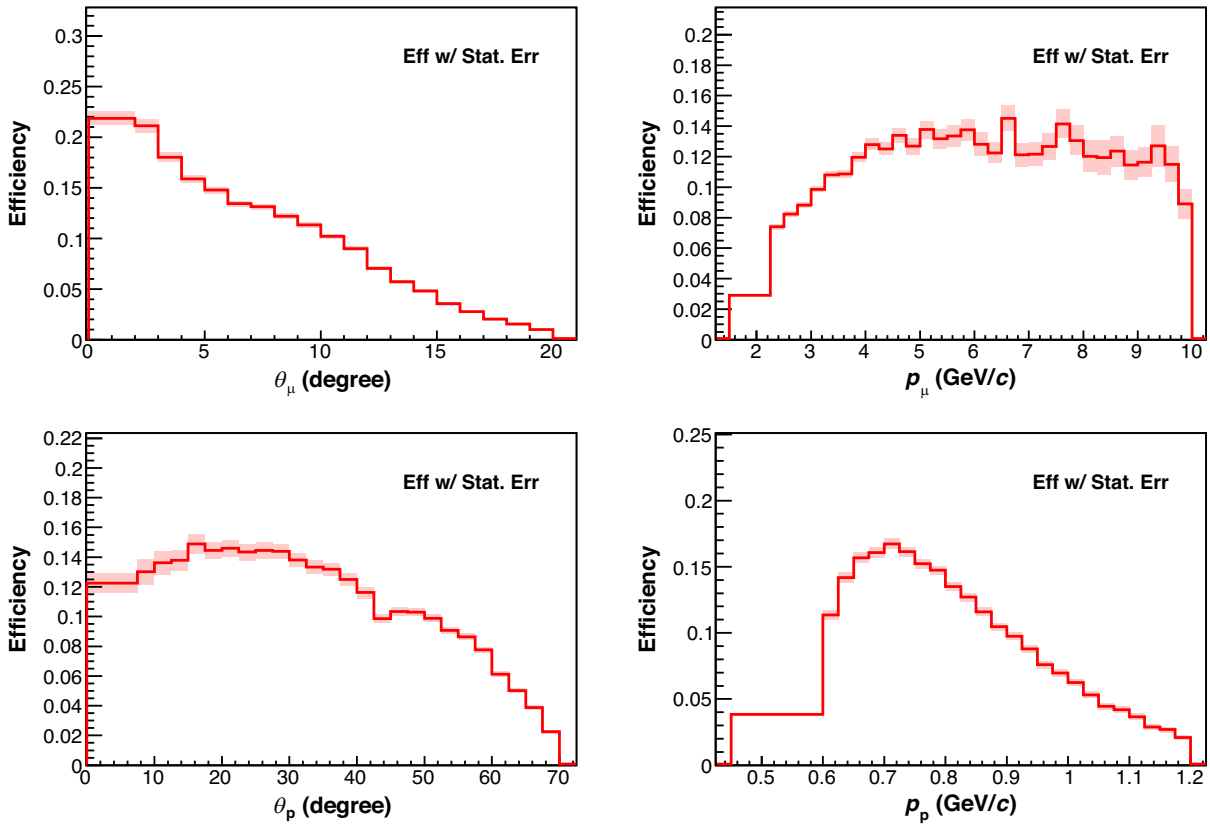

FIG. 4. Muon (top) and proton (bottom) efficiencies as functions of opening angle θ (left) and momentum (right).

Proton identification is done with a track-based $\mathrm{d}E/\mathrm{d}x$ algorithm, which could reconstruct the proton energy (including rescattered protons) to a 5% energy resolution [30]. An additional $\mathrm{d}E/\mathrm{d}x$ selection is applied on these protons to favor ones that interact elastically and contained (ESC) within the CH tracker, which improves the energy resolution to 3% [4,31]. The ESC requirement impacts the selection efficiencies for protons with a higher momentum, which tend to rescatter inelastically more often.

The reconstructed proton energy and angular resolutions are 3% and 2°, while the reconstructed muon energy and angular resolutions are ∼8% and 0.6°. The resolutions of the composite variables δp_{Tx} and δp_{Ty} have been evaluated to be 0.05 GeV/c and 0.06 GeV/c, respectively.

After the event selection, background contributions are estimated using predictions from GENIE 2.8.4. The predicted background consists of events with pions in the final states, which mostly comes from RES and DIS interaction channels. The background is then constrained with a data-driven method with sidebands described in Ref. [32]. The event rate in the signal region and in a representative sideband for δp_{Tx} and δp_{Ty} are shown in Fig. 5. In this figure, the sideband sample shown contains events with off-track visible recoil energy between 0.06 and 0.385 GeV. Four sidebands with different visible recoil energy are used to constrain the backgrounds in bins of proton Q^2_{QE} from 0.15 to 2.0 GeV^2. Separate weights are used for inelastic events with a baryon resonance events and for other, higher W, inelastic backgrounds.

After subtracting the fitted background, the signal fraction is treated with an iterative unfolding procedure [33] to account for the detector resolution [4]. Four iterations are chosen [4] to balance model bias and statistical uncertainties in the unfolded distribution. The stability of the unfolding with four iterations is studied by unfolding different pseudodata sets with model variations different from our assumed cross section model. As an extreme test, one of the variations we study for each of δp_{Tx} and δp_{Ty} puts in a large, nonphysical, asymmetry in the relevant distribution. For each of these pseudodata studies, we compare the consistency of the unfolded pseudodata with the input model assumption as a function of number of iterations. For each pseudodata set, statistical uncertainties are added about the mean data prediction from the mode variation. One thousand pseudodata sets are created for each study. We find that four iterations of unfolding are sufficient to achieve good agreement, where the metric for agreement is the mean χ^2 from the comparisons of unfolded pseudodata to its true distribution. We also verify that the mean χ^2 fails to decrease significantly with additional iterations.

The unfolded data are corrected for the predicted efficiency calculated as a ratio between the predicted

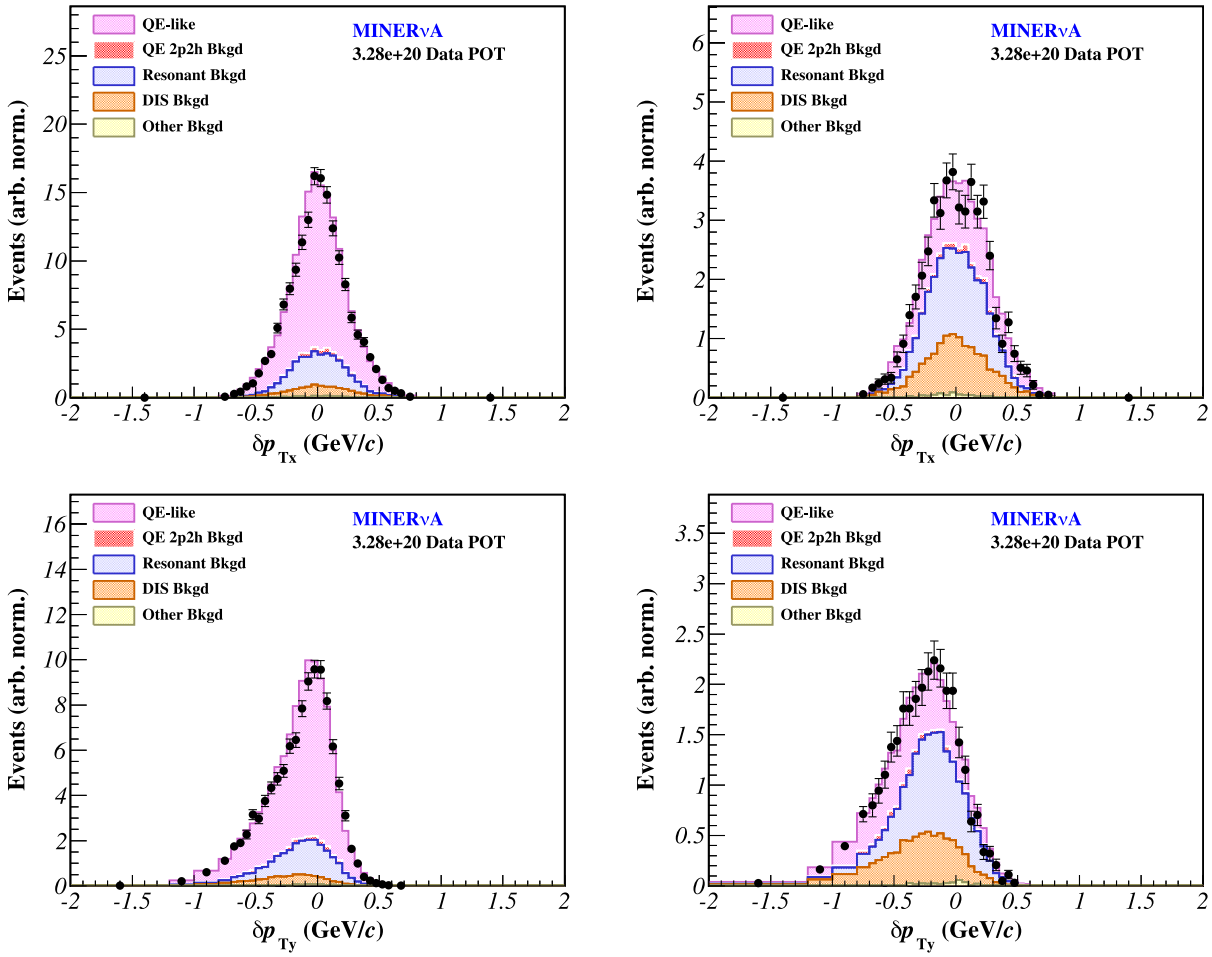

FIG. 5. Reconstructed event rate in the δp_{Tx} signal (top left) and a representative background sideband (top right); the δp_{Ty} signal (bottom left) and a background sideband (bottom right). The background fraction in the signal have been fitted with a data-driven constraint using the sidebands.

and selected number of simulated events in each bin. The efficiencies for δp_{Tx} and δp_{Ty} in the QE region $(-0.5, 0.5)$ GeV/c are constant at 0.1 with 10% relative variations and slowly fall by a factor of 2 over the regions $\pm(0.5, 0.1)$ GeV/c. The flux-averaged differential cross sections are then obtained by normalizing the efficiency-corrected distribution with the number of target nucleons (3.11×10^{30}) and the predicted ν_μ flux.

Uncertainties on δp_{Tx} (δp_{Ty}) result from statistical fluctuations and uncertainties in the NuMI flux prediction, the GENIE modeling, and the detector response. The uncertainties are propagated throughout the cross section extraction procedure, and the results are summarized in Fig. 6.

The final differential cross sections in δp_{Tx} and δp_{Ty} are reported over -0.7 GeV/$c < \delta p_{\mathrm{Tx}}, \ \delta p_{\mathrm{Ty}} < 0.7$ GeV/c. Each broad category of systematic uncertainties, neutrino flux, detector response, and assumed interaction model ("GENIE") ranges between 5% to 10% within this region. The largest contributing factor to uncertainty in the detector response is the tracking efficiency; the largest uncertainty in the neutrino interaction model is the GENIE's model of pion absorption in final state interactions.

VI. RESULTS AND DISCUSSIONS

Model comparison is facilitated with the NUISANCE [34] neutrino interaction cross section comparison package. For the primary comparison with data, we use GENIE 2.12.10 with the Valencia 2p2h model replacing the default empirical 2p2h model. NUISANCE is used to apply the MnvGENIE-v1.0.1 tune that is described above. GENIE 2.12.10 and GENIE 2.8.4 have consistent model implementations. A careful internal MINERvA study indicates the main difference for this analysis is an increase of S^N by 14.8 MeV from changes to the nuclear masses in GENIE.

The unfolded cross section results are shown in Fig. 7. The δp_{Tx} and δp_{Ty} cross sections are in the top and bottom panels, respectively. There are significant non-QE contributions for both distributions. Of these, about half are due to the tuned 2p2h. For each cross section, the QE distribution is broken down into the generated FSI modes.

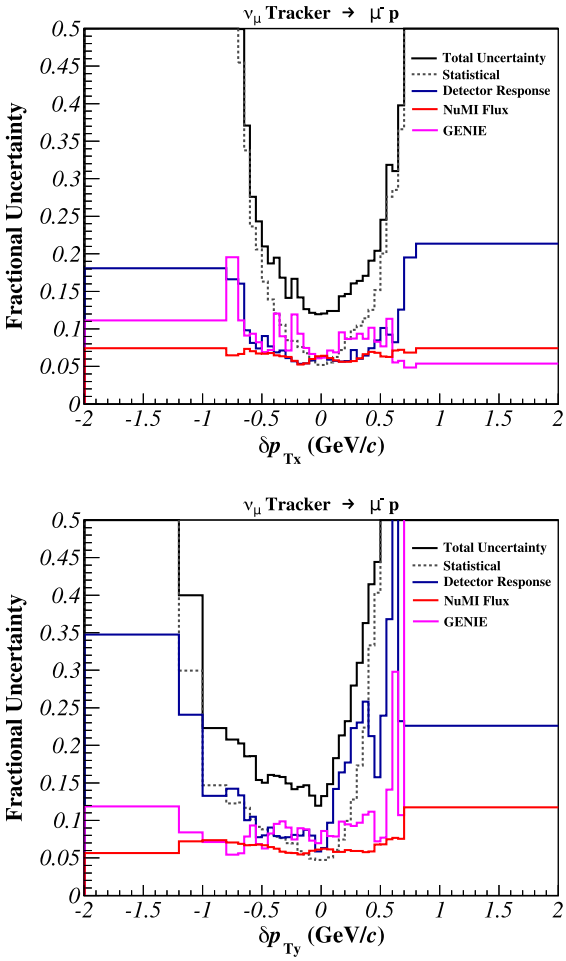

FIG. 6. Uncertainties on the extracted δp_{Tx} (top) and δp_{Ty} (bottom) cross sections.

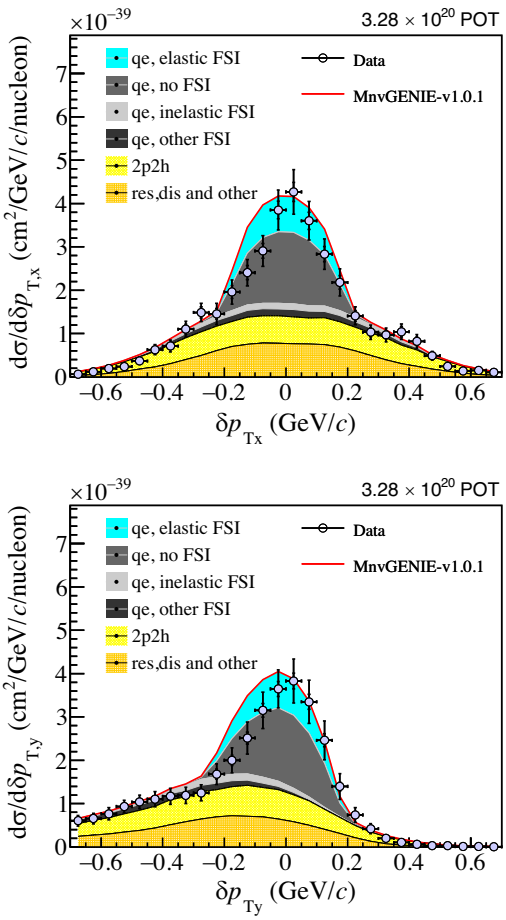

FIG. 7. Differential cross sections in δp_{Tx} (top) and δp_{Ty} (bottom) compared to MnvGENIE-v1.0.1. The MnvGENIE-v1.0.1 histogram is separated into the GENIE defined QE, 2p2h and non-QE event types. The QE region is further separated into the GENIE FSI experienced by the selected proton before exiting the nucleus. The QE elastic FSI regions displayed in the figures are replaced by the no FSI contributions scaled to 51%. Note δp_{Tx} seems to be slightly asymmetric about the center. The δp_{Ty} peak is shifted to the left and has larger width than data.

Here, the GENIE no FSI means the final state nucleon exited the nucleus without interaction; elastic FSI refers to elastic nucleon-nucleon scattering, which typically involves scattering angles less than 10°; and inelastic FSI refers to events with knockout of one or more additional nucleons. The other FSI category includes channels such as the charge exchange multinucleon knockout, and pion production/absorption during nucleon transport. Appendix B describes an error in GENIE's implementation of elastic FSI, the fix we implemented, and the effect of the fix on the predictions and the analysis.

A. Distribution in δp_{Tx}

The measured differential cross sections in δp_{Tx} and δp_{Ty} exhibit a QE peak near 0. If the interaction occurred on a free nucleon, then we would expect a delta function at 0 because the muon and proton final states must balance. The width of the QE peak mostly results from Fermi motion.

The measured cross section in δp_{Tx} in the peak region is wider in the data than in the reference model. While our correction to simulation of elastic FSI does not precisely reproduce a "fixed" elastic FSI, the width of the predicted no FSI contribution itself is larger than the data. If we assume no significant deviation in the non-QE distributions, then the discrepancy could imply an overestimation of the carbon Fermi momentum, or a reduction in the total fraction of the no FSI contribution, or both.

Besides the width discrepancy, the data distribution in δp_{Tx} visually leans towards the positive side.

To measure the significance of the asymmetry, we define the bin-by-bin asymmetry between the positive and negative sides of the differential cross section in δp_{Tx} as

$$A_{\mathrm{Tx}}(|\delta p_{\mathrm{Tx}}|) = \frac{\sigma_+ - \sigma_-}{\sigma_+ + \sigma_-}, \tag{22}$$

where $\sigma_\pm$ is the cross section at either $\pm|\delta p_{\mathrm{Tx}}|$ bin. The resulting distribution is reported in Fig. 8, where

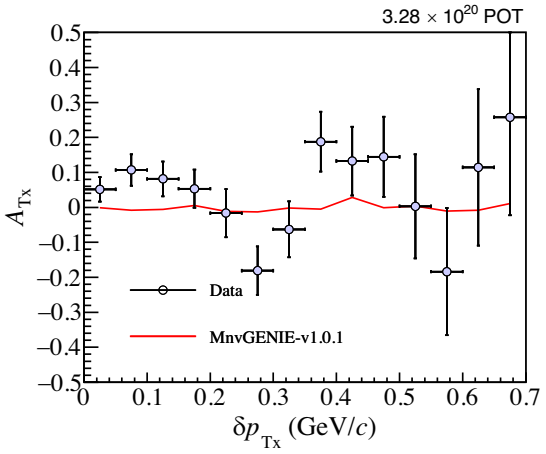

FIG. 8. The bin-by-bin asymmetry in the differential cross sections between $\pm|\delta p_{\mathrm{Tx}}|$ bins [Eq. (22)]. Data are compared to MnvGENIE-v1.0.1, which is representative of the other MC generators used in this study and exhibits no asymmetry.

observation of bin-by-bin asymmetries in the data and their significances in different ranges of δp_{Tx} are reported in Table II. None of the generators used in this study reproduce the asymmetric feature, where MnvGENIE-v1.0.1 is shown as an example.

The total asymmetry is defined as

$$A_{\mathrm{LR}} = \frac{N_- - N_+}{N_- + N_+}, \tag{23}$$

with $N_{-/+}$ being the integrated cross sections on the left/right side of the neutrino-muon plane. The result is

$$A_{\mathrm{LR}} = -0.05 \pm 0.02, \tag{24}$$

where the uncertainty is calculated from the covariance matrix in the Supplemental Material [35].

Such an asymmetry has been suggested to result from the pion absorption contributions to the signal [36]. Measurements of single-pion production at a low energy in deuterium [37] and single-π^0 production by MINERνA [38] have seen positive pion asymmetries about the neutrino-muon plane. The correlated proton angular distributions in this measurement, from baryon resonance production with an unobserved absorbed pion, could exhibit an opposite asymmetry.

TABLE II. χ^2 of asymmetries (A_{Tx}) against no asymmetry case for regions of δp_{Tx} distributions calculated with the covariance matrix.

δp_{Tx} range (GeV)	χ^2/ndf
0.00–0.40	19.9/8
0.40–0.70	4.95/7
0.00–0.70	21.6/15

B. Distribution in δp_{Ty}

Unlike in the δp_{Tx} distribution, we observe a non-QE tail towards the negative δp_{Ty} values. Inelastic events such as 2p2h, resonance, and DIS are inefficient at transferring the lepton momentum to the final state nucleons, since multiple initial states particles are often involved. Therefore, the protons tagged in the non-QE events will in general have less momenta then the muons and are shifted to the left.

The two sets of corrections proposed in Table I are made to the final states muons and protons in MnvGENIE-v1.0.1's CCQE contribution in the MC sample. The effect of correction 1, with U_{opt} only, and correction 2, with both U_{opt} and $|V_{\mathrm{eff}}|$ corrections, are shown in Fig. 9. The effects of U_{opt} is on the order of 2 MeV as it mainly affects nucleons at low kinetic energies.

Almost all of the shift comes from adding the Moniz interaction energy for carbon ($\Delta^{\mathrm{C}}_{\mathrm{GENIE}}$) back to the final state proton and removing the average excitation energy ($\langle E_x \rangle$) from the muon. These corrections alone shift the δp_{Ty} peak 34.2 MeV/c to the right. Application of the optical potential partly cancels the shift, resulting in a net shift of 29.4 MeV/c. However, the addition of the Coulomb effect shifts the peak back, nearly canceling the effect of the optical potential, for a net shift including both effects of 33.9 MeV/c.

The ratios, in the lower panels of Fig. 9, of the corrected models and the data to MnvGENIE-v1.0.1 show the same upward-going trend in the QE peak region between $|\delta p_{\mathrm{Ty}}| < 0.2$ GeV. This trend is characteristic of a peak shift, and the similarities lend confidence to the validity of the theoretically motivated corrections.

Figures 10 and 11 compares NuWro local Fermi gas (LFG), NuWro spectral function (SF), GiBUU, the nominal GENIE, MnvGENIE-v1.0.1, as well as NEUT SF and LFG, distributions normalized to data cross sections. In terms of δp_{Ty}, the nominal GENIE with Nieves 2p2h does not depart much from the overall peak offset seen in MnvGENIE-v1.0.1, the ratio between which is nearly flat. The modifications to the 2p2h fraction, the nonresonant pion reweighting and RPA introduced by the MINERνA tune have little effect on the position of the peak, since their effects are nearly constant at the QE peak. Data to MnvGENIE-v1.0.1 ratio, and in fact, the ratios of all other models to MnvGENIE-v1.0.1, except NuWro LFG follow very similar trends. The NuWro SF and GiBUU models both have better agreements with data while NuWro LFG has overall disagreement in cross section.

The NuWro models include nuclear effects such as Pauli blocking and the Coulomb potential. The NuWro SF model, in particular, includes an effective potential simulating the optical potential. The effective potential is validated against electron scattering data on targets including ^{16}O [39], a nucleus similar to ^{12}C [1]. The NuWro LFG has a larger disagreement with the data. However, the average Fermi

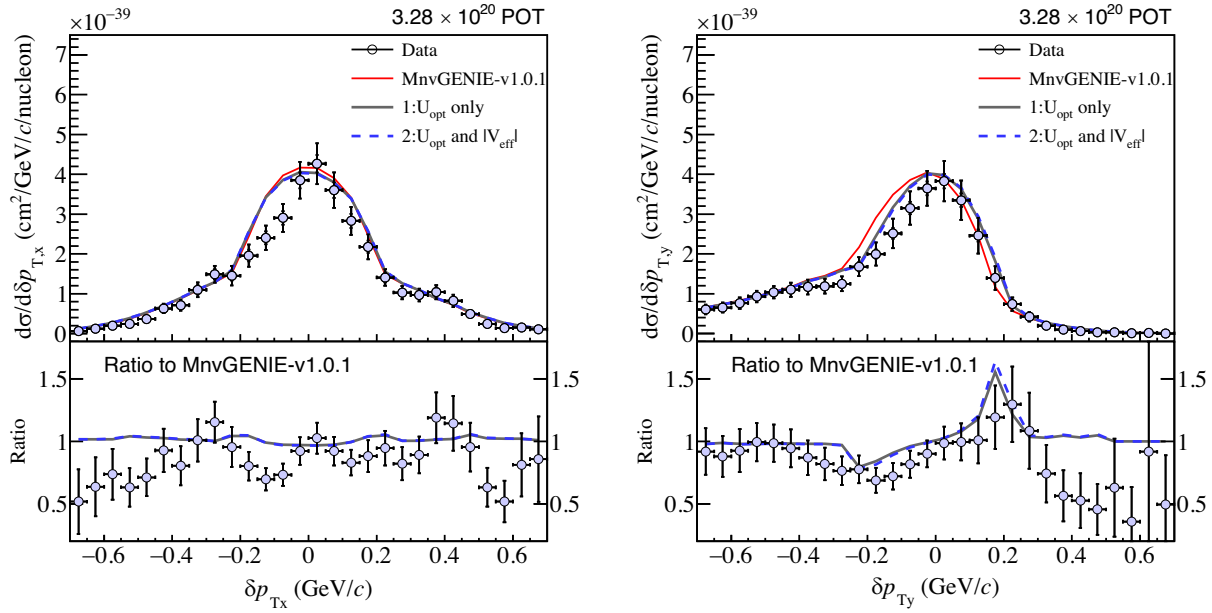

FIG. 9. Differential cross sections in $(\delta p_{\mathrm{Tx}}, \delta p_{\mathrm{Ty}})$ compared with MnvGENIE-v1.0.1 interaction energy corrections, defined in Table I. The corrections minimally affect δp_{Tx}, while bringing the δp_{Ty} peak region into closer agreement with data. Note the similar trends in δp_{Ty} ratios between the corrections and data.

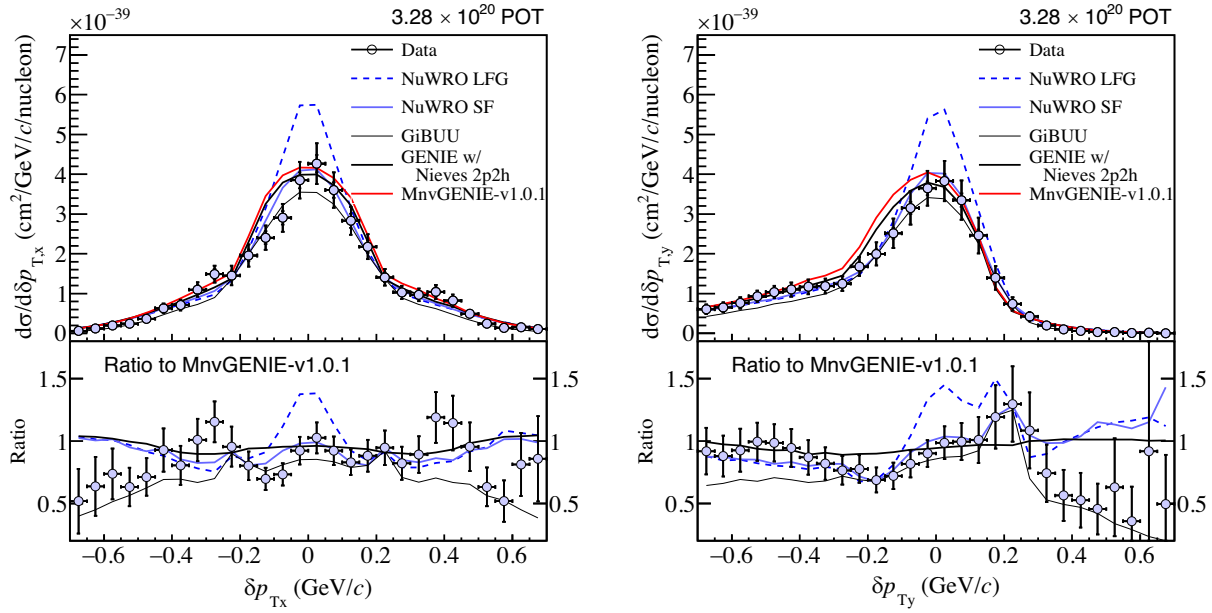

FIG. 10. Model comparisons for NuWro LF, NuWro SF,GiBUU, default GENIE, and MnvGENIE-v1.0.1. Both NuWro SF and GiBUU observe peak shifts consistent with data. NuWro LFG, although more discrepant from the data, describes the narrowness of the data peak well.

motion of the typical LFG models produces a narrower width in the QE peak than that of the Fermi momentum in regular Fermi gas models. This produces a narrower peak more suggestive of the data.

The NEUT SF describes the QE peak location well, while the LFG shifts the peak location by more than 1σ. In fact, NEUT SF describes both δp_{Tx} and δp_{Ty} very well near the peak regions.Unlike the NuWro variant, NEUT LFG predicts wider QE width in δp_{Ty} while at the same time produces width in δp_{Tx} comparable to that of the data.

GiBUU models the initial state nucleons with a local Thomas-Fermi approximation, and the nucleons are bound in a mean-field potential, where Pauli blocking is naturally simulated. The final state particles propagating through the

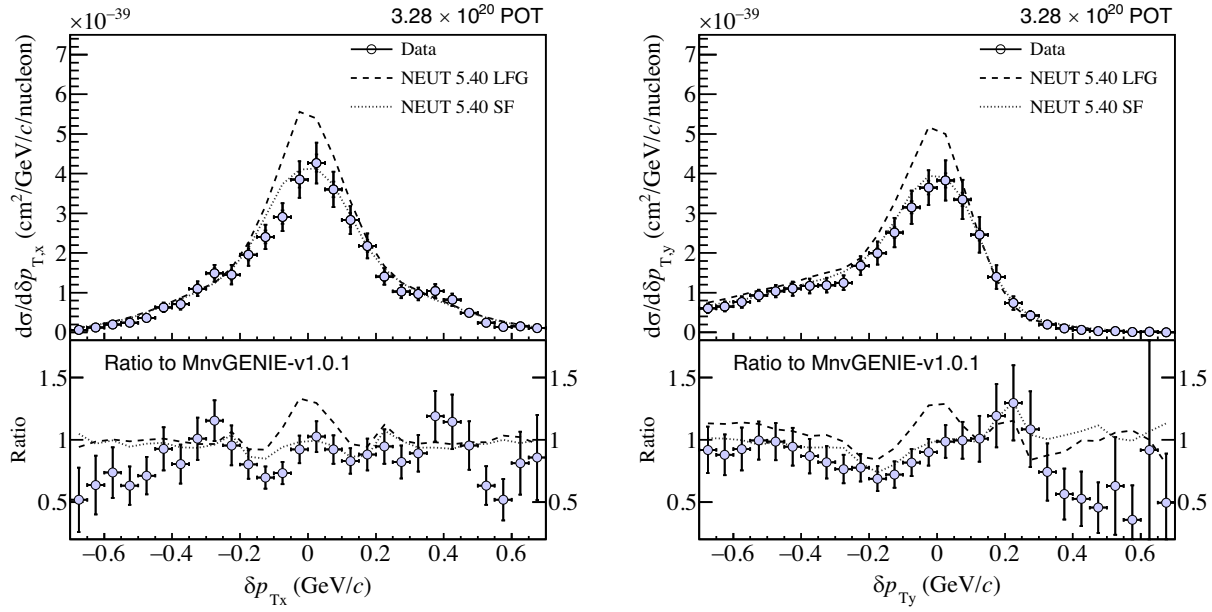

FIG. 11. Model comparisons for NEUT SF and NEUT LFG. The δp_{Ty} distribution in NEUT SF describes the data peak well, while NEUT LFG over-predicts the left side of the peak, leading to a wider peak similar to GENIE.

nuclear medium are subject to a scalar potential that usually depend on both the nucleon momentum and nuclear density [40]. These features of GiBUU do not contribute to an especially superior description of the QE peak. Unrelated to the description of the peak, the tail distributions of the single-TKI quantities are sensitive especially to the 2p2h component and pion production followed by pion absorption with proton knockout. With a lower proton threshold than this analysis, it could include significant amounts of QE events followed by FSI. GiBUU seems to be quite adept at predicting three of the four tails of these signal distributions, while the other generators systematically overestimate these regions.

We investigate the agreement of the δp_{Ty} measurement with model predictions using a weighted average, $\langle \delta p_{\mathrm{Ty}} \rangle$, defined as

$$\langle \delta p_{\mathrm{Ty}} \rangle = \frac{\sum_i \sigma_i \delta p_{\mathrm{Ty}_i}}{\sum_j \sigma_j}, \tag{25}$$

$$V = \frac{\sum_{i,j} \delta p_{\mathrm{Ty}_i} C_{ij} \delta p_{\mathrm{Ty}_j}}{(\sum_k \sigma_k)^2}, \tag{26}$$

where σ_i and δp_{Ty_i} are the cross section and position in the ith δp_{Ty} bin, i, j span over the summed range. The calculation of the variance V takes into account the covariance matrix C_{ij}, which contains the correlated errors between the ith and jth bins. The covariance matrices for δp_{Tx}, δp_{Ty} and the variables reported in Ref. [4] are available as digital data release.

The computation of $\langle \delta p_{\mathrm{Ty}} \rangle$ is sensitive to the range selected due to the underlying non-QE contribution. The $(-0.20, 0.20)$ GeV/c momentum range is chosen because it is dominated by the QE events. The results are summarized in Fig. 12.

For each model, a p value is calculated under the assumption of normally distributed uncertainties on the data. The average peak positions of MnvGENIE-v1.0.1 lie outside 1σ uncertainty range of the data. Measurable shifts

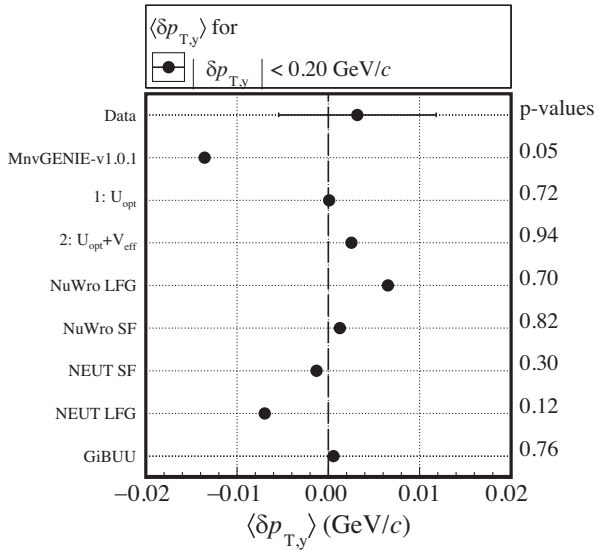

FIG. 12. $\langle \delta p_{\mathrm{Ty}} \rangle$ calculated from the differential cross section within $|\delta p_{\mathrm{Ty}}| < 0.20$ GeV/c. The p value is the probability, assuming normal distribution, that the observed result would have been produced by change from this model.

TABLE III. δp_{Ty}: χ^2 comparisons, POT normalized.

POT normalized	$-0.2--0.1$ GeV	$\mathbf{-0.1-0.0}$ **GeV**	$\mathbf{0.0-0.1}$ **GeV**	$0.1-0.2$ GeV	$-0.2-0.2$ GeV	$-0.7-0.7$
GENIE nominal	41.1/2	**19.0/2**	**0.743/2**	13.5/2	52.9/8	69.5/28
MnvGENIE-v1.0.1	89.0/2	**38.9/2**	**0.184/2**	13.7/2	100/8	72.5/28
1: U_{opt} only	32.4/2	**22.5/2**	**2.73/2**	18.8/2	38.2/8	111/28
2: U_{opt} and V_{eff}	27.7/2	**19.6/2**	**3.71/2**	30.2/2	45.6/8	111/28
NuWro LFG	25.1/2	**159/2**	**130/2**	15.5/2	50.7/8	131/28
NuWro SF	10.6/2	**8.87/2**	**1.46/2**	0.296/2	6.66/8	60.0/28
NEUT 5.40 LFG	43.6/2	**113/2**	**82.6/2**	0.842/2	52.6/8	75.9/28
NEUT 5.40 SF	7.31/2	**9.03/2**	**0.397/2**	0.302/2	4.41/8	54.3/28
GiBUU	1.50/2	**3.81/2**	**6.85/2**	6.04/2	7.70/8	45.0/28

TABLE IV. δp_{Tx}: χ^2 comparisons, POT normalized.

POT normalized	$-0.2--0.1$ GeV	$\mathbf{-0.1-0.0}$ **GeV**	$\mathbf{0.0-0.1}$ **GeV**	0.1–0.2 GeV	$-0.2-0.2$ GeV	$-0.7-0.7$ GeV
GENIE nominal	26.0/2	**31.6/2**	**3.40/2**	4.03/2	26.4/8	69.5/28
MnvGENIE-v1.0.1	38.6/2	**40.4/2**	**4.00/2**	9.11/2	34.5/8	67.2/28
01: U_{opt} only	36.3/2	**35.2/2**	**4.02/2**	9.40/2	35.0/8	67.4/28
02: U_{opt} and V_{eff}	36.2/2	**34.4/2**	**4.03/2**	9.55/2	35.2/8	67.8/28
NuWro LFG	22.2/2	**85.5/2**	**31.4/2**	4.72/2	58.7/8	132/28
NuWro SF	8.79/2	**20.1/2**	**0.831/2**	1.48/2	16.6/8	63/28
NEUT 5.40 LFG	21.4/2	**73.3/2**	**19.0/2**	5.82/2	43.5/8	85.2/28
NEUT 5.40 SF	10.2/2	**24.8/2**	**1.36/2**	0.632/2	17.5/8	58.3/28
GiBUU	1.69/2	**11.7/2**	**7.69/2**	1.27/2	11.9/8	40.6/28

to larger $\langle \delta p_{\mathrm{Ty}} \rangle$ are observed when interaction energy corrections are applied. The shifts are on the order of 15 to 20 MeV/c, consistent with corrections made to the underlying model. The measurements disfavor the default GENIE removal energy implementation, but does not distinguish between the nuclear potential corrections. Among the models NuWro SF, NEUT SF, and GiBUU models are comparable to the data average, while NuWro and NEUT LFGs have larger disagreement with the data. Between them, NEUT LFG peaks outside the measurement uncertainties.

Next, we calculate χ^2 distributions in four consecutive, disjoint δp_{Ty} ranges dominated by QE interactions to illustrate the mismodeling in the MnvGENIE-v1.0.1 simulations. Table. III summarizes the results. The χ^2 in δp_{Ty} for MnvGENIE-v1.0.1 is not symmetric about 0, where the falling side $(0, 0.2)$ GeV/c, with $\chi^2 = 13.7$, is in much better agreement with the data than the rising side $(-0.2, 0)$ GeV/c with $\chi^2 = 89.0$.

The corrections for MnvGENIE-v1.0.1 reduce the model asymmetry, bringing the χ^2 at the left edge from 89.0 to the order of 30. The χ^2 for the right edge increases from 13.7 to 18.8 and 30.2 between corrections 1 and 2. The total χ^2 between $(-0.2, 0.2)$ GeV/c is reduced by more than 50% after the corrections are applied. The overall χ^2s for MnvGENIE-v1.0.1 is 72.5, while both its corrections are 111 for 28 degrees of freedom.

Other Fermi gas-based models, such as NuWro LFG and NEUT LFG, in general have better χ^2 than the GENIE variations. The NuWro LFG χ^2 in the edges are more consistent with each other, at 25.1 and 15.5, respectively. The NEUT LFG, on the other hand, seems to suffer from model asymmetry similar to MnvGENIE-v1.0.1, but the cause might be due to a systematic excess in the cross section predicted in the negative tail of the δp_{Ty} distribution, as shown in Fig. 11. The tail is dominated by non-QE interactions. In contrast, spectral function models and GiBUU predict δp_{Ty} very well.

We also show the χ^2 distributions for δp_{Tx} in Table IV. Across all of the models, we observe bias in the χ^2 as a result of the asymmetry in data that we previously characterized by the measurement of A_{LR} in Eq. (24).

VII. SUMMARY AND OUTLOOK

The variables δp_{Tx} and δp_{Ty} are measured on the CH target in MINERνA. We expect δp_{Tx} to be sensitive to the Fermi momentum in QE, and there is tension between data and MC. The data are narrower than the GENIE model, as is true of most models other than a simple Fermi gas. The measurement also shows a statistically marginal proton asymmetry in δp_{Tx} of -0.05 ± 0.02. This asymmetry, if truly nonzero, might be attributed to pion absorption events included in the signal. No model in current event generators

predicts an asymmetry. Future measurements could verify the presence of this asymmetry.

The observable δp_{Ty} shows sensitivity to the interaction energy implemented in nuclear models. In particular, the measurement, which is based on GENIE, disfavors the default GENIE implementation of the interaction energy on carbon. This implementation lacks the excitation energy while subtracts an extra Moniz interaction energy from the final state proton. The average peak positions between GENIE and data differ by more than 1.5σ. Approximate corrections accounting for the excitation energy and Moniz interaction energy bring the average peak position within 1σ of the data. This measurement is not precise enough to distinguish the more subtle nuclear effects such as the optical potential and the Coulomb potential. To first order, more statistics could reduce the overall uncertainties in the distributions. Further improvements in the overall uncertainties need to come from better constrained flux, detector response, and signal model, especially in the modeling of pion absorption in the nucleus.

We have compared different Monte Carlo models with respect to δp_{Tx} and δp_{Ty}. The measurements are based on the MnvGENIE-v1.0.1 tune of GENIE, which removes the elastic FSI components in GENIE on top of the MnvGENIE-v1 base tune. This modification subsequently impacts the single-TKI measurements performed in Ref. [4]. The elastic FSI is discussed in Appendix B. The Supplemental Material [35] to this paper contains an update to the single-TKI results presented in Ref. [4] based on this modification.

Future MINERνA analysis using the medium energy [41] data set will benefit from higher statistics, which will enable examination of correlations between δp_{Tx}, δp_{Ty}, and other variables. In particular, probing the correlation of the asymmetry in δp_{Tx} with other variables may shed light on its origin. Other targets in MINERνA and future liquid argon experiments could make measurements of $(\delta p_{\mathrm{Tx}}, \delta p_{\mathrm{Ty}})$, and the single-TKI variables in general, to test models on other nuclei.

ACKNOWLEDGMENTS

This work was supported by the Fermi National Accelerator Laboratory under US Department of Energy Contract No. DE-AC02-07CH11359, which included the MINERνA construction project. Construction support was also granted by the United States National Science Foundation under Grant No. PHY-0619727 and by the University of Rochester. Support for participating scientists was provided by NSF and DOE (USA), by CAPES and CNPq (Brazil), by CoNaCyT (Mexico), by Proyecto Basal FB 0821, CONICYT PIA ACT1413, Fondecyt 3170845 and 11130133 (Chile), by DGI-PUCP and UDI/VRI-IGI-UNI (Peru), by the Latin American Center for Physics (CLAF), by Science and Technology Facilities Council (UK), and by NCN Opus Grant No. 2016/21/B/ST2/01092 (Poland). We thank the MINOS Collaboration for use of its near detector data. We acknowledge the dedicated work of the Fermilab staff responsible for the operation and maintenance of the beam line and detector and the Fermilab Computing Division for support of data processing.

APPENDIX A: DERIVATIONS OF GENIE CORRECTIONS

The purpose of this correction is to modify the prediction of the GENIE event generator for a different value of E_x^N. In general, this correction could modify both the energy and three momentum transferred to the nucleus but have the freedom to pick some quantity, which should be conserved event-by-event in this correction. We choose the magnitude of the three momentum transfer, q_3. Changes to q_0, Q^2, and angles and energies of the final state muon and proton follow. Denote the change in q_0 to be

$$\tau = E_x^N - |U_{\mathrm{opt}}[(\mathbf{k}+\mathbf{q_3})^2]| + |V_{\mathrm{eff}}^{\mathrm{P}}|, \tag{A1}$$

and let

$$M'_N = M_N - S^N - \frac{\langle \mathbf{k}^2 \rangle}{2M_{A-1}^2}. \tag{A2}$$

Then the energy conservation at the vertex in GENIE is

$$q_{0\mathrm{GENIE}} + M'_N = \sqrt{(\mathbf{k}+\mathbf{q}_3)^2 + M_P^2}, \tag{A3}$$

comparing to Eq. (7), we obtain

$$q_0 \approx q_{0\mathrm{GENIE}} + \tau. \tag{A4}$$

The difference in energy transfer manifests on the outgoing muon energy,

$$E_\nu - E_\mu = E_\nu - E_\mu^{\mathrm{GENIE}} + \tau, \tag{A5}$$

we obtain the energy correction to the GENIE muon,

$$E_\mu = E_\mu^{\mathrm{GENIE}} - \tau. \tag{A6}$$

The outgoing proton energy in GENIE is

$$E_P^{\mathrm{GENIE}} = \sqrt{(\mathbf{k}+\mathbf{q}_3)^2 + M_P^2} - \Delta_{\mathrm{GENIE}}^{\mathrm{nucleus}}. \tag{A7}$$

Comparing to the right-hand side of Eq. (7), we obtain

$$E_P = E_P^{\mathrm{GENIE}} + \Delta_{\mathrm{GENIE}}^{\mathrm{nucleus}} - |U_{\mathrm{opt}}| + |V_{\mathrm{eff}}^{\mathrm{P}}|. \tag{A8}$$

As noted above, this correction conserves energy and assumes $|\mathbf{q}_3|$ is constant. The fractional change to the Q^2 of the system is approximately $\Delta Q^2/Q^2 = \tau/M_N$. For our sample, $\tau \approx 10$ MeV, produces a 1% shift in Q^2, which causes changes to the hard scattering cross section $\lesssim 1\%$.

We can also evaluate how changes in the angle of the muon and the proton that are neglected in the GENIE correction would affect the prediction. The muon momentum before and after the correction are

$$\mathbf{p}_\mu = p_\mu \begin{pmatrix} 0 \\ \sin(\theta) \\ \cos(\theta) \end{pmatrix}, \tag{A9}$$

$$\mathbf{p}'_\mu = (p_\mu - \tau) \begin{pmatrix} 0 \\ \sin(\theta + \delta) \\ \cos(\theta + \delta) \end{pmatrix}. \tag{A10}$$

Solving the equation $|\mathbf{p}_\nu - \mathbf{p}_\mu|^2 = |\mathbf{p}_\nu - \mathbf{p}'_\mu|^2$ for δ to first order in τ, we have

$$\delta \approx \tau \left(\frac{1}{E_\nu \sin(\theta)} - \frac{1}{p_\mu \tan(\theta)} \right). \tag{A11}$$

Note that the effect on the angle could become significant at small θ, but in this region $E_\nu - E_\mu$ becomes small, and in this region, the recoiling protons in quasielastic events are also soft that such they do not enter our sample. For our events, $\delta \lesssim 1.5$ mrad.

For an interaction, the $\mathbf{p}_\mu$ and $\mathbf{p}_P$ are balanced at the vertex. Changing the θ must elicit a compensating change in the proton angle to conserve the momentum. In our correction, we neglect the small changes of angles above. This introduces a very small error in the calculation of δp_{Ty} for events that pass our selections, particularly the proton momentum cut. This error decreases with Q^2 and is at most 0.25 MeV for $Q^2 = 0.2$ GeV^2. Therefore, the simplifying assumption in our modification of GENIE that the muon and proton angles do not change is justified.

APPENDIX B: GENIE ELASTIC FSI SIMULATION

This section will discuss the elastic FSI prediction and the fixes to it in more detail.

The prediction from MnvGENIE-v1 in δp_{Tx} has three distinct regions shown in Fig. 13: a non-CCQE tail beyond $|\delta p_{\mathrm{Tx}}| \gtrsim 0.2$ GeV$/c$, a no FSI CCQE dominated region in $0.2 \gtrsim |\delta p_{\mathrm{Tx}}| \gtrsim 0.1$ GeV$/c$, which reflects the Fermi momentum, and an elastic FSI peak at $|\delta p_{\mathrm{Tx}}| \lesssim 0.1$ GeV$/c$. The GENIE elastic FSI is sharply peaked and much narrower than the underlying Fermi gas distribution. Since the protons in the elastic FSI peak follow the no FSI distribution before the FSI simulation, we expect the width of the elastic FSI distribution to be at least as large as that of the no FSI distribution.

Hints of the unphysical nature of the angular distribution already appeared in the original single-TKI analysis reported in Ref. [4]. MINERνA uses the default GENIE

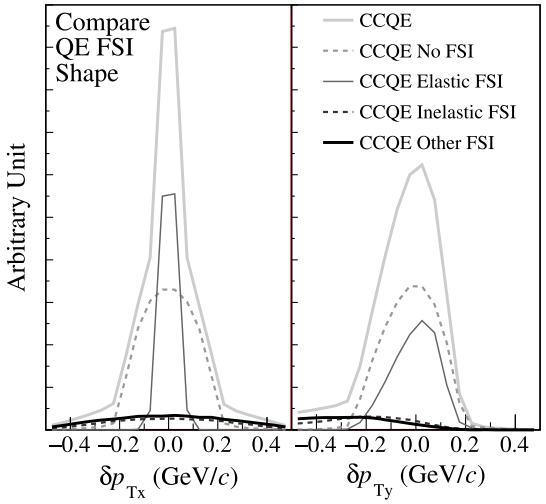

FIG. 13. GENIE FSI modes breakdown for CCQE events. The noninteracting fraction is symmetric and preserves the Bodek-Ritchie Distribution, while the GENIE elastic FSI appears accelerated with respect to the transverse momentum transfer q_T.

configuration of version 2.12 which uses the "hA" model for FSI. In this model, every nucleon experiences exactly one of the following fates: 1) no FSI, 2) charge exchange with single nucleon knockout, 3) elastic hadron + nucleus scattering, 4) inelastic single nucleon knockout, 5) multinucleon knockout (including pion absorption), and 8) pion production. An advantage of this model is that a reweighting technique can be used to modify the relative mix of fates without fully regenerating the Monte Carlo samples. This is convenient for studying FSI systematic effects with an analysis, similar to the existing FSI uncertainties available with the GENIE hA model.

The routine used to calculate all FSI reactions involving a two body scatter contains (in GENIE versions 2.6 to version 3.0.6) a mistake that affects hA fates "2" and "4" (nucleon knockout, with and without charge exchange) and fate "3" (elastic hadron nucleus scattering) for both protons and pions. Fate "3", combined with quasielastic events and single-TKI variables, create the largest in observable distributions [42].

The primary effect is on the angular distribution of the scattered hadrons. In the QE case, the original code causes too few of the most highly transverse protons, which have low efficiency to be tracked in the MINERνA planar design. It also produces a population, especially of QE events, with a very narrow angle distribution, and in quantities derived from those angular distributions, like many of the single-TKI observables. The angular distribution relative to the lepton and other hadrons are separately affected. This combination affects the predicted distributions presented in Ref. [4] in multiple ways. In addition, the resulting hadrons pick up an acceleration of up to 2 MeV. This is smaller than most hadronic energy uncertainties and has a negligible role in selection or calorimetry. Instead,

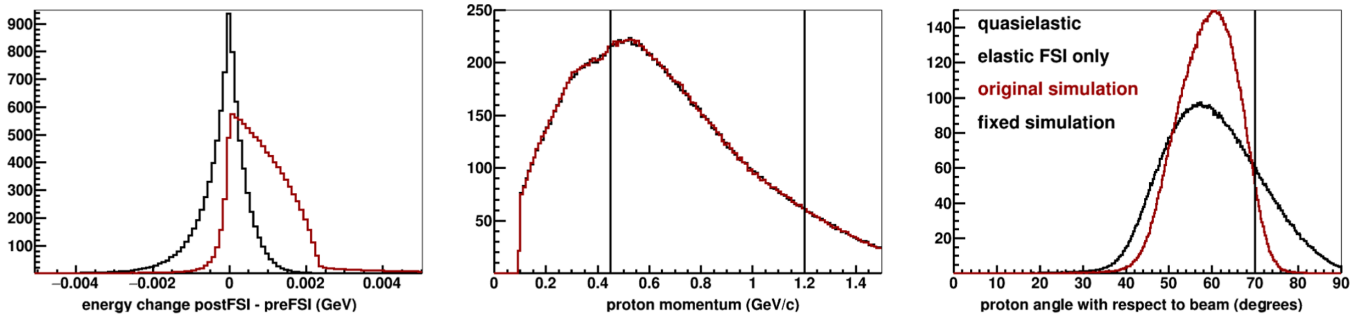

FIG. 14. Comparison of the effect of fixing the GENIE code and comparing key QE proton distributions. Left: Proton acceleration showing the old code produced less than 2 MeV shift. Middle: the small energy shift has negligible effect on the momentum distribution. Right: a major distortion of the angle distribution is what affects the single-TKI analyses; the correct angle distribution is similar to protons (not shown) which had no FSI. Before the fix, this and other distributions based on proton angle such as Fig. 13 are too narrowly peaked [42].

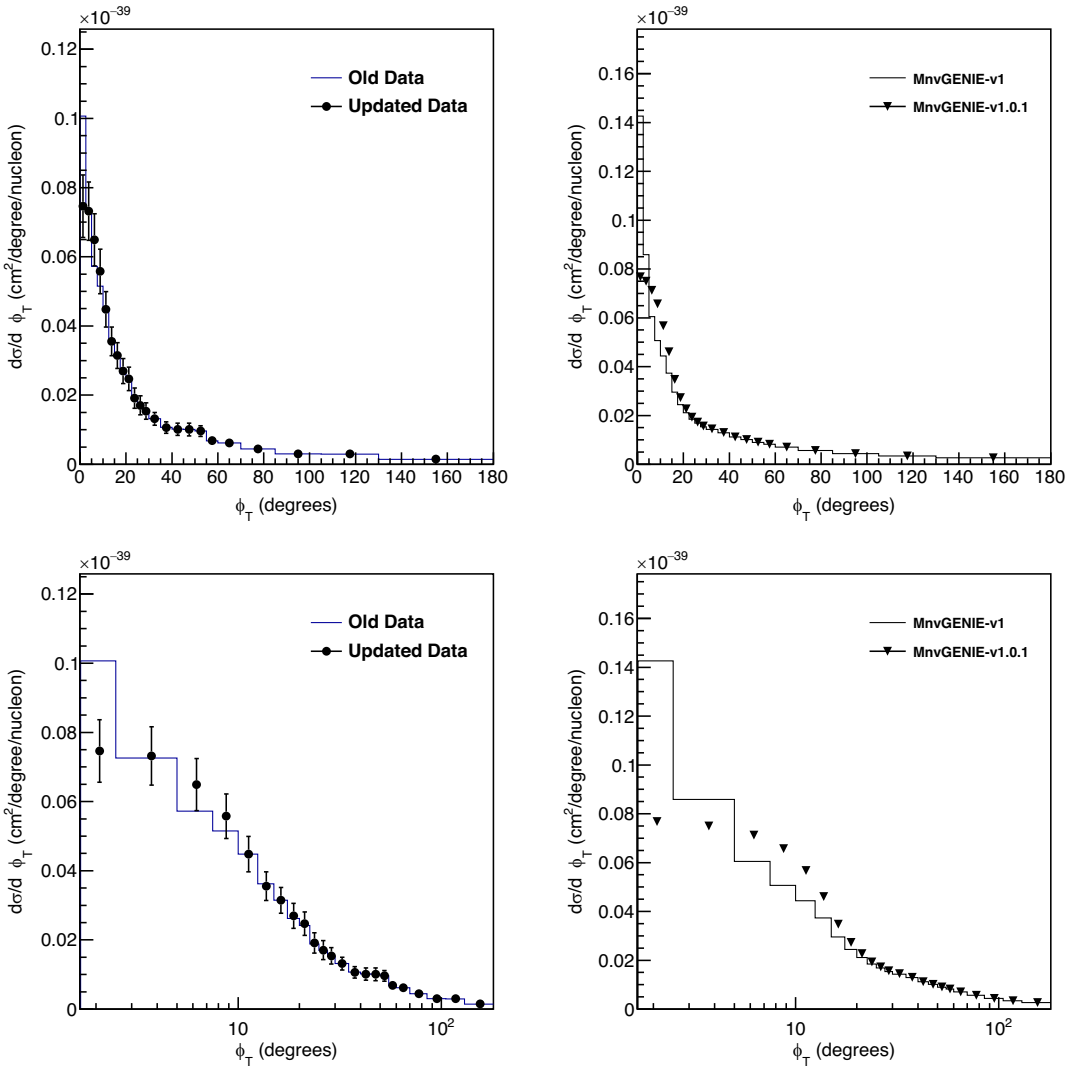

FIG. 15. $\delta\phi_T$ is the angular projection of proton transverse momentum. The original FSI code produces a peak at $0(rad)$ indicating protons were being produced in the reaction plane more often than Fermi motion would give. The first cross section data point is the only one that shifted by more than 2σ.

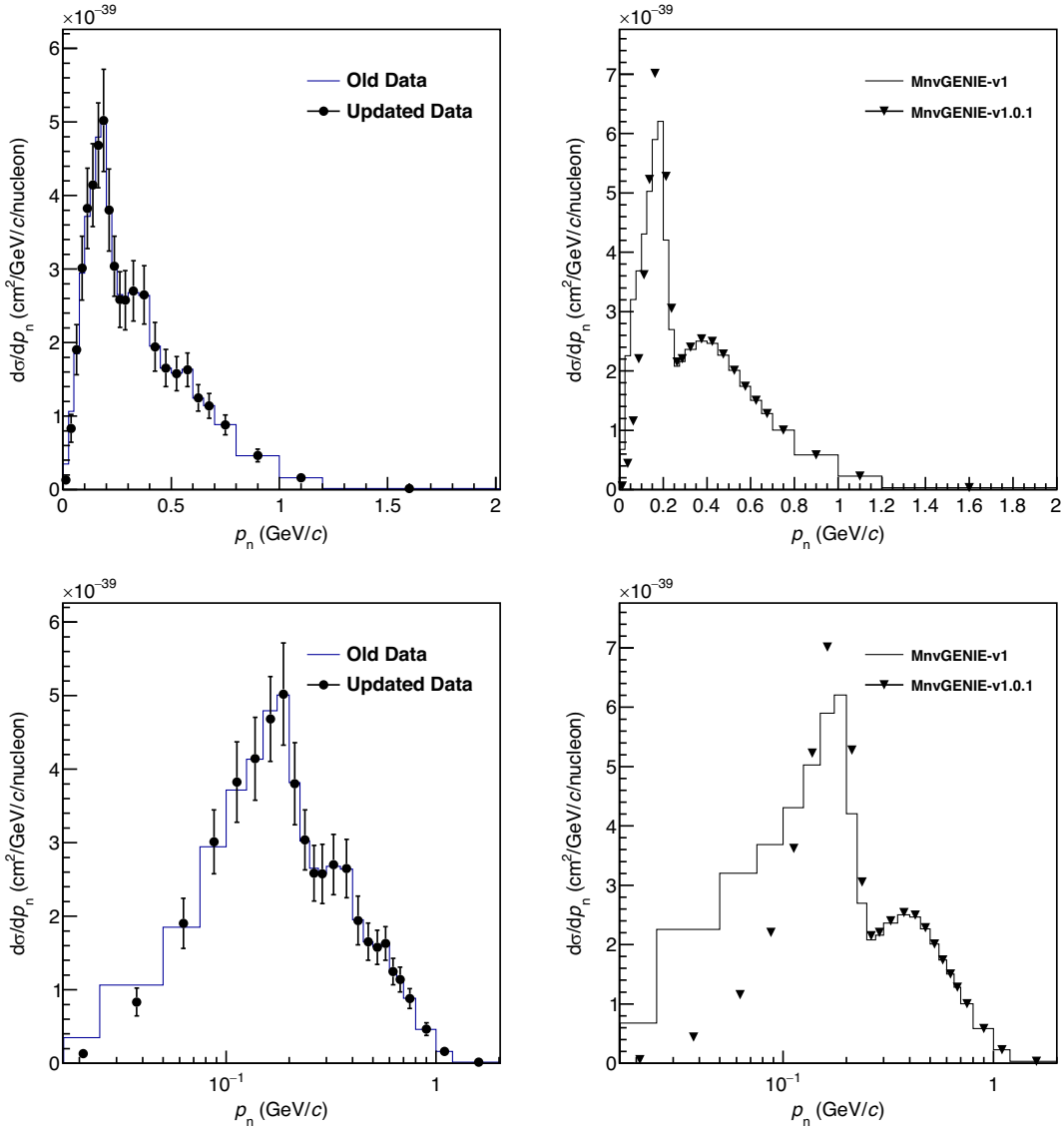

FIG. 16. The inferred initial neutron momentum, p_n, extracted before and after the elastic FSI reweight. Only the first bin differ more than 2σ.

it appears as an unphysical population in all single-TKI populations in Ref. [4]. The largest effects of the distorted input model, after performing the iterative unfolding procedure, are on the acceleration angle and the coplanarity angle.

The study reported in Ref. [42] suggests reweighting up the no FSI fate and removing the elastic fate contributions will sufficiently mimic the proton distributions in a fixed code without having to regenerate all MC. Figure 14 shows the effect of fixing the GENIE code and comparing key QE proton distributions. The reason is that the intended elastic scattering angle for protons and neutrons is always small: 90% would be less than 8°. For this analysis, the weights are only applied to GENIE quasielastic events; the distortion of angles for nonquasielastic events with multiple hadrons has a small effect on these distributions.

Figures 15 and 16 shows $\delta\phi_T$ and p_n, respectively. The left plot shows the comparison between data extracted using the MnvGENIE-v1 (old data) and the MnvGENIE-v1.0.1 (updated data). The right plot compares the two MC models. All model distributions are modified significantly, but the extracted cross section shifts are only significant in the first bins of $\delta\phi_T$ and p_n.

TABLE V. χ^2 of the old and updated data compared to MnvGENIE-v1.0.1.

Variables	Old data	Updated data	d.o.f.	Δ in reduced χ^2
p_n	103	96.8	26	0.24
$\delta\alpha_T$	25.6	26.4	13	−0.062
$\delta\phi_T$	100	77.1	24	0.95
δp_T	48.1	30.0	26	0.70

Table V compares the old and updated data to the MnvGENIE-v1.0.1 model. The two data extractions are consistent within 1 unit of reduced χ^2. The two data for $\delta\phi_T$ and p_n differ significantly only in the first bin, but the effect on χ^2 is small.

The Supplemental Material [35] to this paper contains an update to the single-TKI results presented in Ref. [4] based on this modification.

Citation of the new cross sections should include this paper and the original paper [4] describing the full method.

[1] A. Bodek and T. Cai, Eur. Phys. J. C **79**, 293 (2019).
[2] K. Abe *et al.* (T2K), Phys. Rev. Lett. **121**, 171802 (2018).
[3] X.-G. Lu, L. Pickering, S. Dolan, G. Barr, D. Coplowe, Y. Uchida, D. Wark, M. O. Wascko, A. Weber, and T. Yuan, Phys. Rev. C **94**, 015503 (2016).
[4] X.-G. Lu *et al.* (MINERνA Collaboration), Phys. Rev. Lett. **121**, 022504 (2018).
[5] K. Abe *et al.* (T2K Collaboration), Phys. Rev. D **98**, 032003 (2018).
[6] C. Andreopoulos (GENIE Collaboration), Acta Phys. Pol. B **40**, 2461 (2009).
[7] Y. Hayato, Acta Phys. Pol. B **40**, 2477 (2009).
[8] C. Juszczak, J. A. Nowak, and J. T. Sobczyk, Nucl. Phys. B, Proc. Suppl. **159**, 211 (2006).
[9] O. Buss, T. Gaitanos, K. Gallmeister, H. van Hees, M. Kaskulov, O. Lalakulich, A. B. Larionov, T. Leitner, J. Weil, and U. Mosel, Phys. Rep. **512**, 1 (2012).
[10] K. Gallmeister, U. Mosel, and J. Weil, Phys. Rev. C **94**, 035502 (2016).
[11] P. E. Hodgson, Rep. Prog. Phys. **34**, 765 (1971).
[12] R. A. Smith and E. J. Moniz, Nucl. Phys. **B43**, 605 (1972); **B101**, 547(E) (1975).
[13] L. Aliaga *et al.* (MINERνA Collaboration), Nucl. Instrum. Methods Phys. Res., Sect. A **743**, 130 (2014).
[14] P. Adamson *et al.*, Nucl. Instrum. Methods Phys. Res., Sect. A **806**, 279 (2016).
[15] L. Aliaga *et al.* (MINERνA Collaboration), Phys. Rev. D **94**, 092005 (2016); **95**, 039903(A) (2017).
[16] A. Bodek and J. L. Ritchie, Phys. Rev. D **23**, 1070 (1981).
[17] C. H. Llewellyn Smith, Phys. Rep. **3**, 261 (1972).
[18] D. Rein and L. M. Sehgal, Ann. Phys. (N.Y.) **133**, 79 (1981).
[19] A. Bodek and U. K. Yang, Nucl. Phys. B, Proc. Suppl. **112**, 70 (2002).
[20] D. Ruterbories *et al.* (MINERνA Collaboration), Phys. Rev. D **99**, 012004 (2019).
[21] C. E. Patrick *et al.*(MINERνA Collaboration), Phys. Rev. D **97**, 052002 (2018).
[22] J. Nieves, R. Gran, F. Sanchez, and M. J. Vicente Vacas, arXiv:1310.7091.
[23] R. Gran, J. Nieves, F. Sanchez, and M. J. V. Vacas, Phys. Rev. D **88**, 113007 (2013).
[24] J. Schwehr, D. Cherdack, and R. Gran, arXiv:1601.02038.
[25] P. A. Rodrigues, J. Demgen, E. Miltenberger *et al.* (MINERνA Collaboration), Phys. Rev. Lett. **116**, 071802 (2016).
[26] C. Wilkinson, P. Rodrigues, S. Cartwright, L. Thompson, and K. McFarland, Phys. Rev. D **90**, 112017 (2014).
[27] P. Rodrigues, C. Wilkinson, and K. McFarland, Eur. Phys. J. C **76**, 474 (2016).
[28] J. Nieves, J. E. Amaro, and M. Valverde, Phys. Rev. C **70**, 055503 (2004); **72**, 019902(E) (2005).
[29] R. Gran, arXiv:1705.02932.
[30] T. Walton *et al.* (MINERνA Collaboration), Phys. Rev. D **91**, 071301 (2015).
[31] X.-G. Lu and M. Betancourt (MINERνA Collaboration), J. Phys. Conf. Ser. **888**, 012120 (2017).
[32] T. Walton, A measurement of the Muon neutrino charged current quasielastic-like cross section on a hydrocarbon target and final state interaction effects, Ph.D. Thesis, Hampton University, 2014, https://doi.org/10.2172/1155872.
[33] G. D'Agostini, Nucl. Instrum. Methods Phys. Res., Sect. A **362**, 487 (1995).
[34] P. Stowell *et al.*, J. Instrum. **12**, P01016 (2017).
[35] See Supplemental Material at http://link.aps.org/supplemental/10.1103/PhysRevD.101.092001, for comparisons of single-TKI variables after correcting the mismodelling in GENIE's elastic FSI.
[36] T. Cai, X.-G. Lu, and D. Ruterbories, Phys. Rev. D **100**, 073010 (2019).
[37] G. M. Radecky *et al.*, Phys. Rev. D **25**, 1161 (1982).
[38] O. Altinok *et al.* (MINERνA Collaboration), Phys. Rev. D **96**, 072003 (2017).
[39] A. M. Ankowski and J. T. Sobczyk, Phys. Rev. C **77**, 044311 (2008).
[40] T. Leitner and U. Mosel, Phys. Rev. C **81**, 064614 (2010).
[41] P. Adamson *et al.*, Nucl. Instrum. Methods Phys. Res., Sect. A **806**, 279 (2016).
[42] L. Harewood and R. Gran, arXiv:1906.10576.